Scholars Journal of Engineering and Technology

Abbreviated Key Title: Sch J Eng Tech ISSN 2347-9523 (Print) | ISSN 2321-435X (Online) Journal homepage: https://saspublishers.com

CFD Simulations of Supersonic Jets Impinging on Axisymmetric and Double-Wedge Deflector of Satellite Launch Vehicle

R. C. Mehta1*

¹Department of Aeronautical Engineering, Noorul Islam Centre for Higher Education, Kumaracoil 629180 India

DOI: https://doi.org/10.36347/sjet.2025.v13i09.002 | Received: 12.07.2025 | Accepted: 19.09.2025 | Published: 22.09.2025

*Corresponding author: R. C. Mehta

Department of Aeronautical Engineering, Noorul Islam Centre for Higher Education, Kumaracoil 629180 India

Abstract Original Research Article

The flowfield of overexpanded and under expanded supersonic jets on an axisymmetric and double-wedge jet deflector has been numerically studied by solving axisymmetric and three-dimensional compressible Euler equations using a finite volume method in conjunction with three-stage Runge-Kutta time-marching scheme. The numerical simulation is carried out for the nozzle exit Mach number 2.2 and 3.1 ambient to exit pressure ratio of 1.2, 1.0, 0.8 and 0.6 and distance between nozzle exit to deflector apex ratio of 2, 3, 4 and 5 time the nozzle exit diameter. The impinging jets is characterized defined by many flow discontinuities, such as cone shock, Mach disk, reflected shock and jet boundaries. The numerical simulations consist of pressure and Mach contour and surface pressure distributions. Influence of nozzle operating pressure ratio and nozzle exit plane to deflector surface have been investigated using computational fluid dynamics CFD analysis. Flowfield produced due to impingement of cold air jet on a jet deflector has been studied using CFD and computed static pressure distribution along the deflector surface. The numerical results are compared with the available experimental data and shows good agreement between them. The numerical scheme will be useful for the design of jet deflector during the lift-off phase of a satellite launch vehicle.

Keywords: CFD; Inviscid flow; Mach disc; Supersonic flow; Schlieren picture; Shock wave; Impinging jet; Launch pad; Axisymmetric and wedge deflector.

Copyright © 2025 The Author(s): This is an open-access article distributed under the terms of the Creative Commons Attribution 4.0 International License (CC BY-NC 4.0) which permits unrestricted use, distribution, and reproduction in any medium for non-commercial use provided the original author and source are credited.

NTRODUCTION

Jet interaction with the launch pad as well as with the satellite launch vehicle itself, considered an important and complex fluid dynamic problem during the lift-off of a launch vehicle. The aspects to be considered are - spread-out of exhaust gases away from the launch pad through a suitable jet deflector, pressure, acoustic and heat loads on the jet deflector that may effects on the vehicle caused by jet deflection from the launch pad. It is generally known that the shape of deflector surface is the main factor affecting the diversion performance of the flame deflector. For rocket vehicle launch, it is normal practice to deflect the exhaust jet away from the launch complex in a controlled manner with a suitable shape and positioned deflector device. There are several kinds of defectors, including closed defectors with a closed duct/trench and open defectors without one. According to the main deflection direction, deflectors could be divided into single-sided and multiple-sided defectors. Different defectors show different acoustic efficiency [1]. Large rockets are commonly launched from launch pads which include

service structure, the launch platform and the deflector system as shown in Fig. 1. The launch platform lies beneath the launch vehicle with cutouts (for strap-on) at some specific locations. The exhaust gases pass through these cutouts, impinges onto the deflector and deflects exhaust gases away from the vehicle.

The impingement of underexpanded, axisymmetric rocket motor exhausts and cold jets on flat plate has been studied by Cobbald [2]. Main purpose of the jet deflector of a rocket launch vehicle is to deflect jet away from the launch complex in a controlled manner to protect delicate parts of rocket vehicle, hazards for personnel.

Wedge-shaped deflector [3] (launch complex 34 for Saturn vehicle) was formed by joining together two-unidirectional deflector. Sub-scale static tests conducted by NASA on a double wedge deflector for Saturn booster ($T_o = 3572$ °K, $T_e = 1811$ °K, $M_e = 3.12$ and $\gamma = 1.2$). Office National d'Etudes et de Recherches Aèropatialales (ONERA) has conducted 1/20 scaled model of the Ariane launch vehicle [4] to evaluate the

acoustical field at take-off and pressure distributions at the bottom of the vehicle.

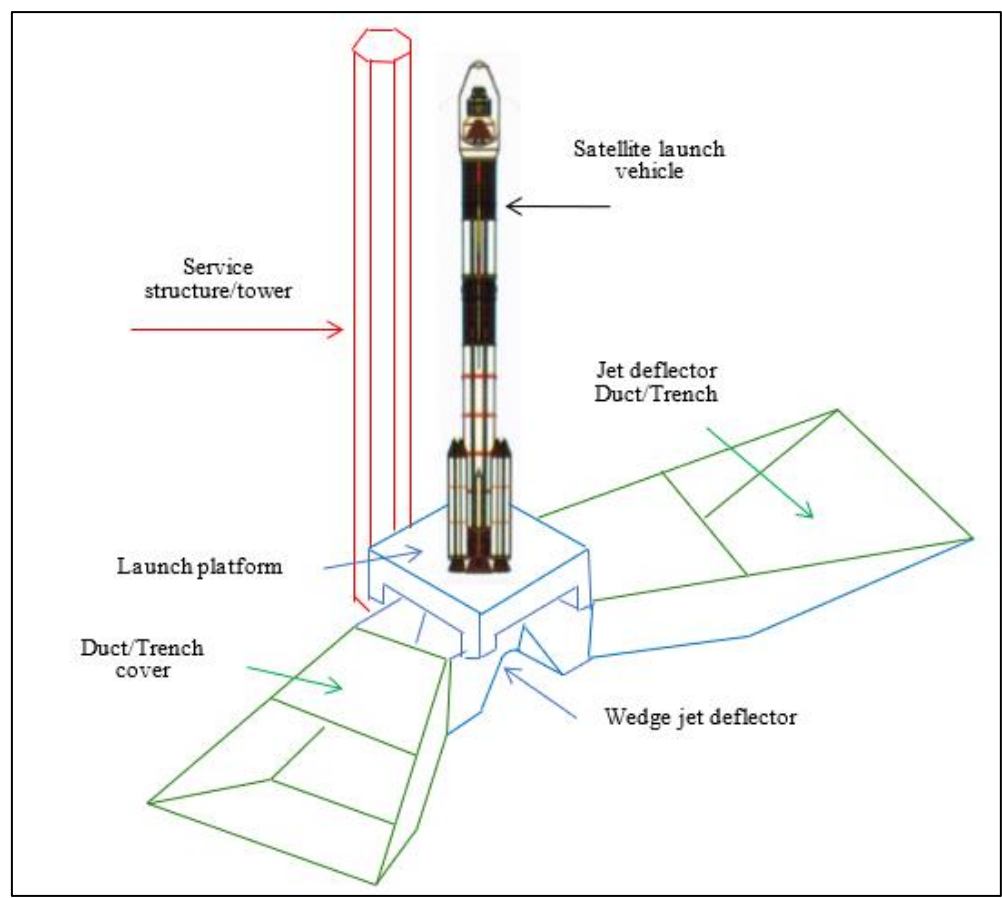


Fig. 1: Schematic sketch of double-wedge deflector of a typical satellite launch vehicle

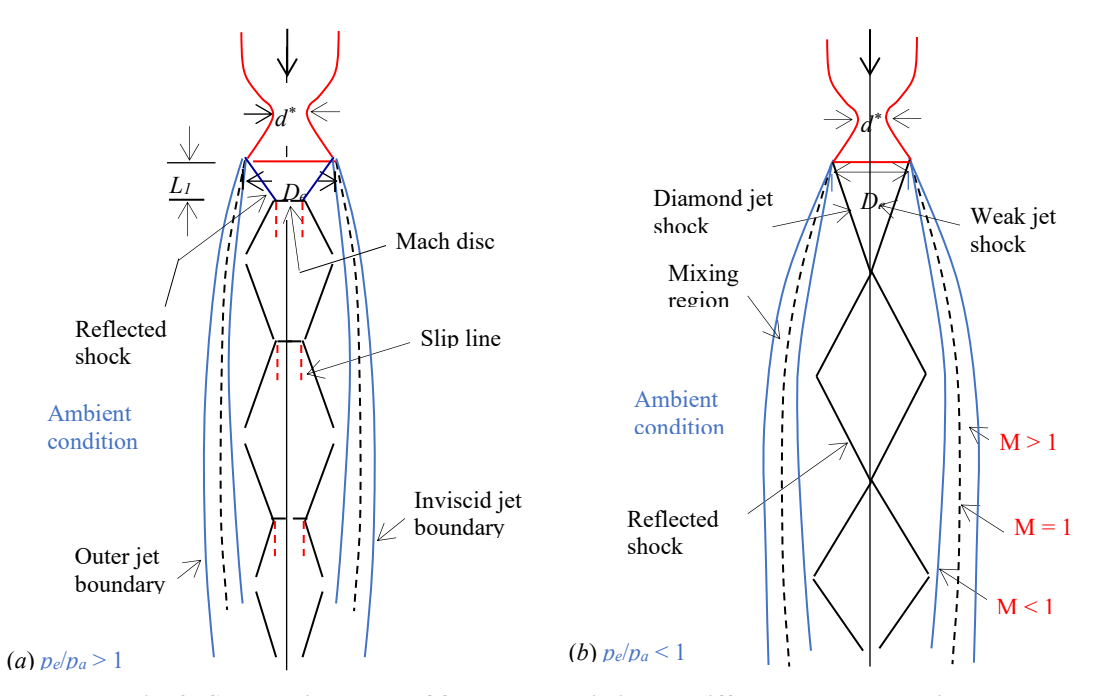


Fig. 2: Schematic sketch of free supersonic jets at different pressure ratio

Lamont and Hunt [5] carried out experimental investigations of supersonic jet impingement on an inclined plate through pressure measurements and

shadowgraph visualizations, and they observed that the plate inclination has a strong influence on the pressure distribution. Nakai *et al.*, [6] investigated supersonic jet

impingement on an inclined plate with different inclination angles, pressure ratios, and nozzle-plate distances with pressure-sensitive paints for surface pressure measurements and schlieren photography for flow visualization. The combined in influences of the pressure ratio, impingement distance and inclined angle on impinging flowfields jets have been conducted by Nakai et al., [7]. Zhou et al., [8] have analyzed the fourengine liquid rocket flowfield impingement on deflector during the launching phase. Jiang et al., [9] presented an overview on progresses and perspectives of the jet impingement research for rocket launching. Numerical simulations [10] have been performed to investigate the exhaust plume impinging on the wedge-shaped and cone-shaped deflectors. A comparative analysis between different jet deflector shows that the cone-shaped deflector achieves better performance as compared to wedge shaped deflector. Numerical solutions of the impingement of an underexpanded axisymmetric supersonic jet on a flat plate at varied angles have been carried out by Wu et al., [11] and Kim et al., [12]. Computational analysis of underexpanded jets on inclined plate is carried out by Mcllory et al., [13]. Numerical simulations have been performed by Zhou et al., [14] to investigate the exhaust gas impinging on the wedge-shaped and cone-shaped deflectors. They found that the maximum pressure and temperature in the wedge-shaped deflector are, respectively, 37.2% and 9.9% higher than those in the cone-shaped flame deflector. Experiments [15] were carried out at different nozzle stand-off distances L/D_{e} from the launch pedestal, simulating the lift-off of the launch vehicle. Using the reasonable shape of the flame deflector can reduce the adverse effects caused by the recirculation or backdraft of rocket exhaust gas [16, 17].

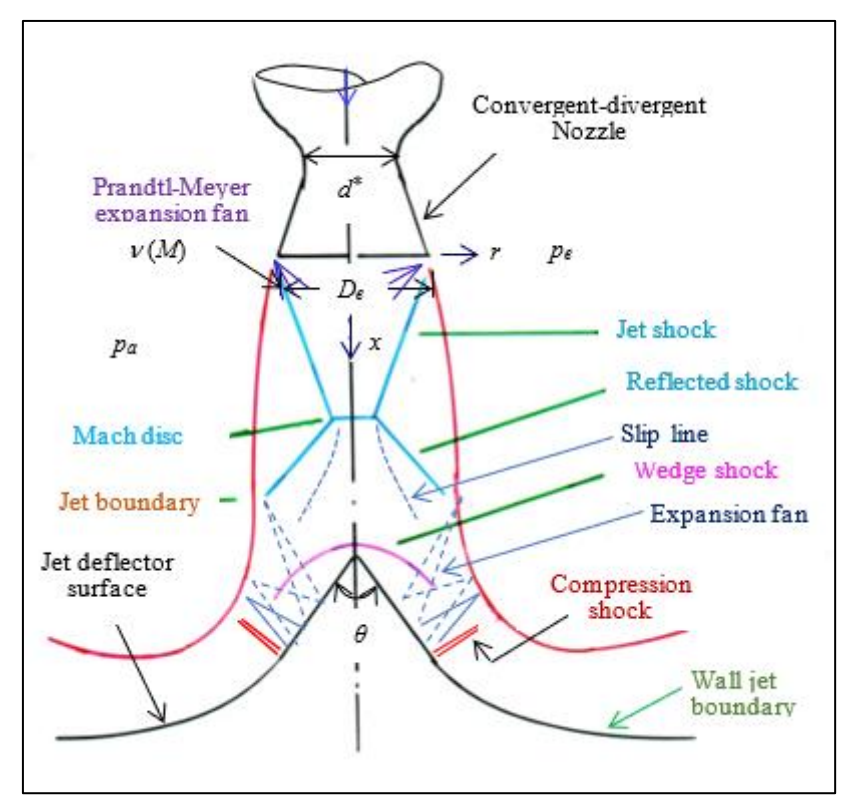


Fig. 3: Schematic sketch of flowfield of free-supersonic jets impinging over a deflector

Numerous experimental studies have been reported which uses cold air jets instead of actual rocket exhaust for investigating impingement flows. The studies with cold air jets have provided a valuable insight into flow processes occurring in cold jet impingement flows. Numerical analysis impingement of supersonic on axisymmetric deflector at $M_e = 2.2$, $p_e/p_a = 1.2$ and 0.8 and $X_w/D_e = 2$ and 3 have been carried out by Prasad *et al.*, [18]. Experimental pressure distribution have been used to compute boundary layer thickness, friction factor using compressible boundary layer equations for $M_e = 3.1$, $p_e/p_a = 0.81$ and $X_w/D_e = 3$ to 5 by Prasad *et al.*, [19]. Mehta [20] has carried out numerical simulation of double wedge supersonic jet deflector for $M_e = 2.2$, p_e/p_a

= 0.8 and X_w/D_e = 3. An analysis of impinging supersonic jets have been simulated for various operating conditions of launch vehicle [21]. Jiang *et al.*, [22] have written an excellent review article on impinging jets during rocket launching.

It turns out that flow fields of the normal impinging jet are similar to those in the free jet in a certain region near the nozzle exit, which is called the free jet region and classified as over expaded *i.e.*, $p_e/p_a < 1$ and under expaded jets *i.e.* $p_e/p_a > 1$. Figure 2(a) and (b) illustrates schematic sketch of free supersonic jets at pe/pa < 1 and pe/pa > 1, respectively. For an under expanded jet, the flow expands at first until its pressure

balances with the ambient pressure. Then, the flow becomes over-expanded and induces compression waves, which converge to form the intercepting shocks. For an overexpanded jet, in other words, the pressure at the nozzle exit is lower than ambient pressure, oblique shocks would be generated by the compression from the ambient fluid.

The compression waves at the nozzle exit converge to form oblique shock waves as shown in Fig. 2 (a), which subsequently intersect and reflect. A supersonic flow is developed in the nozzle, compression waves at the nozzle exit converge into an oblique shock wave, which then intersects and reflects at the shear layer boundary, forming shock-cell structures. The axial jet undergoes repetitive compression-expansion cycles, forming periodic shock-cells characterized by a series of compression and expansion waves. These shock-cells arise from the pressure and velocity imbalance between the jet and the ambient environment, with each cell representing a local adjustment to equilibrium conditions. The region downstream of the free jet region and close to the plate is called the impingement region.

An expansion fan develops at the nozzle exit, inducing the intersection and subsequent reflection of the compression waves as shown in Fig. 2 (b). Constrained by the deflection angle and pressure matching, the flow evolves continuously, generating shock-cell structures. As the expanding flow interacts with the shear layer boundary, compression waves converge to form an oblique shock wave, and the Mach reflection appears on the axis of rotation under high pressure-gradient. A slipstream originates from the triple point, which separates the subsonic flow downstream of the Mach disk and the supersonic flow following the reflected oblique shock.

The exhaust gas impinges onto the launch platform and produces complex flow structures as illustrated in schematic sketch in Fig. 3. During this stage, the exhaust gases interacts with the deflector surface. The impingement jet is on the wedge deflector

$$\frac{\partial U}{\partial t} + \frac{\partial F}{\partial x} + \frac{1}{r} \frac{\partial (rG)}{\partial r} + \frac{S}{r} = 0$$

 $\frac{\partial U}{\partial t} + \frac{\partial F}{\partial x} + \frac{1}{r} \frac{\partial (rG)}{\partial r} + \frac{S}{r} = 0$

 $U = \begin{bmatrix} \rho \\ \rho u \\ \rho v \\ \rho e \end{bmatrix}, \ F = \begin{bmatrix} \rho u \\ \rho u^2 + p \\ \rho uv \\ (\rho e + n)u \end{bmatrix}, \ G = \begin{bmatrix} \rho u \\ \rho uv \\ \rho v^2 + p \\ (\rho e + n)u \end{bmatrix}, \ S = \begin{bmatrix} 0 \\ 0 \\ p \\ 0 \end{bmatrix}$

with the ideal gas assumption, the pressure and total enthalpy can be expressed as

$$\rho e = \frac{p}{(\gamma - 1)} + \frac{1}{2}\rho(u^2 + v^2) \tag{2}$$

where γ is assumed to be 1.4.

2.2 Numerical scheme

where

The numerical algorithm employs finite volume discretization scheme. Spatial and temporal terms are shock wave, exhaust gas jet boundary, Mach disk, reflected shock, plate shock as delineated in schematic sketch of the flow field based on schlieren picture [19] in Fig.3. Characteristics of the impinging jets are different from the free jets as seen in Figs. 2 and 3. Thus, there is considerable complexity in the

characterized by many discontinuities such as barrel

fluid dynamic problem that arises during the lift-off of a launch vehicle. Though one can tackle specific design problems through a combination of suitably tailored subscale experiments and computational fluid dynamics CFD methods, there is clearly a demand for obtaining a much better understanding of the fluid dynamic aspects involved and their effects on pressure loads. The newly emerging field of computational fluid dynamics can play a significant role in this along with carefully conducted subscale tests. The paper employed a CFD approach to simulate the impingement of the supersonic jet on an axisymmetric and a double wedge jet deflector at various operating condition of rocket engine. The numerical simulations are carried out employing axisymmetric and three-dimensional compressible timedependent Euler equations. The performance of axisymmetric deflector with double-wedge deflector are compared for identical model dimension and operating conditions of exhaust gases. The present study will be useful for the structure and aerodynamic design of a launch vehicle deflector.

2. Governing fluid dynamics equations 2.1 Axisymmetric fluid dynamics equations

Effects of turbulence mixing terms are neglected in the present numerical simulations. The assumption of large Reynolds number and low Knudsen number is relatively acceptable, except for the region in vicinity of jet boundary, where substantial mixing take place. Attributed to the highly nonlinear nature of these flows, the compressible inviscid equations give a reasonable model for the physics of fluids. To capture and discontinuities, the time-dependent compressible axisymmetric Euler equations are written in conservation form as

(1)

decoupled applying method of lines. The computational region is divided into a number of quadrilateral grids. The conservative variable U within each grid is evaluated by their average value at quadrilateral grid centre. The inviscid flux vectors F and G, and source vector S of Eq. (1) are evaluated on each side of the grid.

The above numerical scheme needs additions of artificial dissipation terms to preserve odd-even decoupling and to controlled numerical oscillations in vicinity of severe flow gradients. The blend of second and fourth differences provided third-order background dissipation in smooth regions of the flow and first-order dissipation in shock waves. Fourth-order dissipation is added everywhere in the computational region where the solution is smooth, but are 'switch-off' in the region of shock wave. The artificial dissipation model adopted in the present paper is based on the work of Jameson *et al.*, [23].

The spatial discretization described above reduces the governing fluid dynamics equations to semi-discretized ordinary differential equations. The integration is carried out using a two-stage Runge-Kutta

time-stepping scheme [23]. In order to minimize the computation time, the evaluation of the dissipation term is carried out only at the first stage, and then frozen for the subsequent stages. The numerical scheme is stable for a Courant number ≤ 1 . A local time step is used accelerate convergence to achieve steady state numerical solution by advancing the time step at each grid point with the maximum time step allowed by the local Courant–Friedrichs–Lewy (CFL) condition.

2.3 Boundary conditions

Four types of boundary conditions are required for the computation of flow field, i.e., deflector surface, inflow, outflow, and symmetric conditions. They are prescribed as follows: At the deflector wall slip boundary condition is imposed and at the out-flow boundary, the two tangential velocity components are extrapolated from the interior, while at the inflow boundary they are specified as having far field values. The boundary conditions of axisymmetric jet deflector are in Fig. 4.

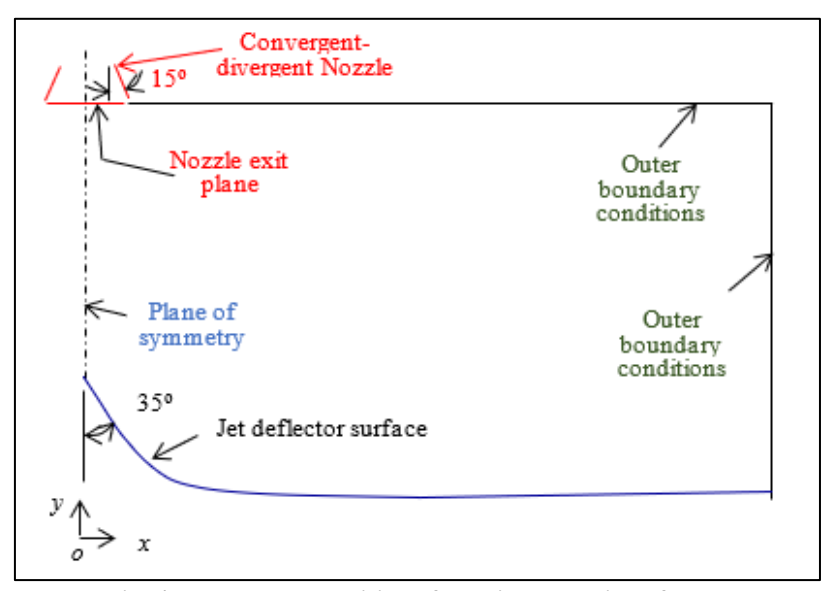


Fig. 4: Boundary conditions for axisymmetric deflector

2.4 Dimension of Nozzle and axisymmetric deflector model

The convergent-divergent nozzles were designed for producing jet exit M_e of 2.2 and 3.1 for the exit diameter D_e of 30 and 23 mm, respectively. Geometrical detail of the axisymmetric deflector is shown in Fig. 5. The nozzle was having a semi-divergent cone angle of 15°. The jet deflector model consists of a cone apex angle of 70° and a tip blunt radius R_I of $0.13D_e$. Further downstream a curvature of radius R_2 of $1.2D_e$ is provided at a location of $r = 0.7D_e$, where r is distance measured from the model axis. The deflector has a base diameter of $8D_e$.

2.5 Computational grid over axisymmetric deflector

Supersonic jets exhausting into a normally stationary external stream are computed using inviscid

flow solver developed inhouse. The initial jet radius is equal to the exit radius i.e. equal to 0.5D_e. A simple algebraic grid generation program is used to generate computational grid in computational domain. Due to axisymmetric nature of the problem, the computations are carried out on only one half of the jet. The computations were used about 600 equally spaced grid points in the axial direction. A grid refinement was carried out in the radial direction by employing 60, 80, 100 and 120 mesh points. The present numerical simulation was carried out on 120 × 600 grid points which were selected after extensive grid independent test. The convergence criterion to steady-state is taken (between two successive iterations) $|\rho^{n+1} - \rho^n| \le 10^{-4}$, where n is an iterative index. The steady-state is achieved after about 30000 iterations.

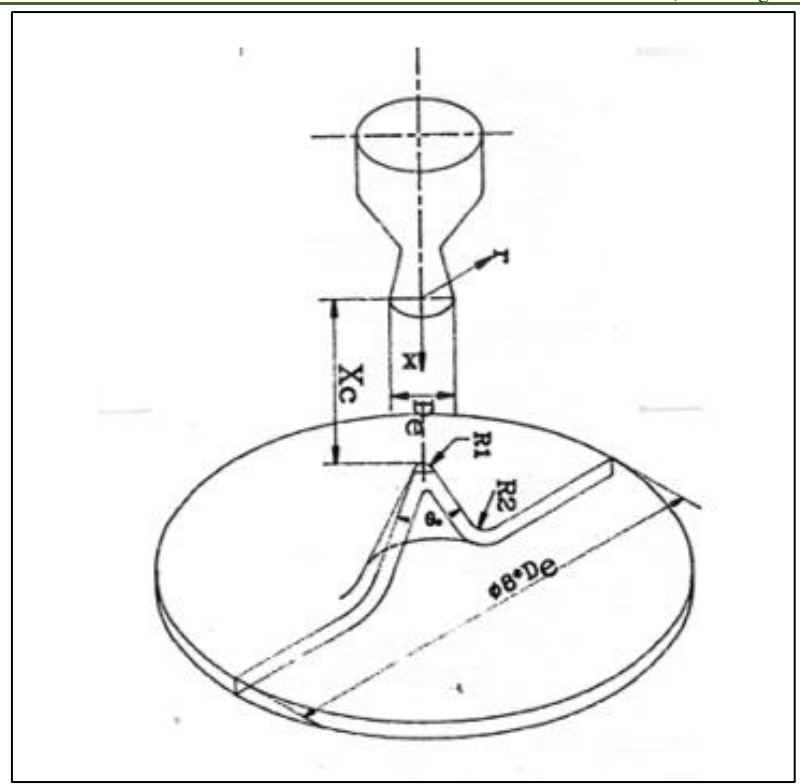


Fig. 5: Geometrical details of the axisymmetric deflector

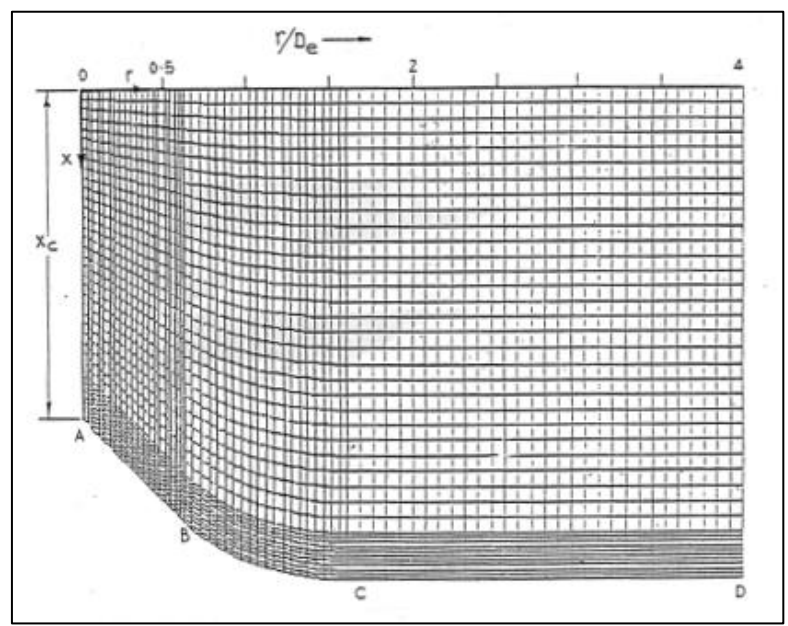


Fig. 6: Computational grid for the axisymmetric plane in flow domain

A simple algebraic grid generation program is used to generate the mesh in the computational region, ABCDEFG as depicted in Fig. 6. GA is the jet axis of line of symmetry. ABCD is the deflector wall, (boundary condition)and DE and EF are free boundaries. For a solid wall the flow properties in the image cell are taken as those of the adjacent boundary cell, except that the normal component of the velocity is reflected to ensure the impermeability conditions. The image cell is taken while applying symmetry condition in the case of

axisymmetric flow. For supersonic outflow, all of the properties in the cell are extrapolated from the adjacent interior cells. At the nozzle exit FG,

2.6 Three-dimension Euler Equations

The equations solved are the Euler equations describing the flow of an inviscid, compressible fluid. To allow the capture of shocks and the discontinuities phenomena, the three-dimensional time-dependent Euler equations are written in conservation vector form as

$$\frac{\partial \mathbf{U}}{\partial t} + \frac{\partial F}{\partial x} + \frac{\partial G}{\partial y} + \frac{\partial H}{\partial z} = 0 \tag{3}$$

where

$$\boldsymbol{U} = \begin{bmatrix} \rho \\ \rho u \\ \rho v \\ \rho w \\ \rho e \end{bmatrix}' \boldsymbol{F} = \begin{bmatrix} \rho u \\ \rho u^2 + p \\ \rho u v \\ \rho u w \\ (\rho e + p) u \end{bmatrix}, \boldsymbol{G} = \begin{bmatrix} \rho v \\ \rho u v \\ \rho v^2 + p \\ \rho v w \\ (\rho e + p) v \end{bmatrix}, \boldsymbol{H} = \begin{bmatrix} \rho w \\ \rho u w \\ \rho v w \\ \rho w^2 + p \\ (\rho e + p) w \end{bmatrix}$$

are the U state vector conserved quantities with ρ , u, v, w and e denoting the density, Cartesian velocity components, and the specific total internal energy, respectively, and inviscid flux vectors, F, G and H in the Cartesian coordinate. With the ideal gas assumption, the pressure and total enthalpy can be expressed as

$$e = \frac{p}{(\gamma - 1)\rho} + \frac{1}{2}(u^2 + v^2 + w^2)$$
 (4)

where γ is the ratio of specific heats.

2.7 Numerical scheme

To facilitate the spatial discretization in the numerical scheme, the governing fluid dynamics equation (3) can be written in the integral form over a finite volume as

$$\frac{\partial}{\partial t} \int_{\Omega} \mathbf{U} d\Omega + \int_{\Gamma} (\mathbf{F} + \mathbf{G} + \mathbf{H}) \vec{n} d\Gamma = 0$$
 (5)

where Ω is the arbitrary control volume with the closed boundary $\partial\Omega$ and control surface Γ , and outward normal facing unit vector n. The domain is divided into a finite number of hexahedral cells, and Eq. (3) is applied to each cell. The state variables U are volume-averaged values. The discretization of Eq. (3) follows discretization in space and time is done separately. A

finite volume cell is specified by eight corners as shown in Fig. 7. The discrete values of the flow quantities are calculated at the centre of the cell. Simple vector information can be used to obtain side and surface vectors relationship along with the computational cell volume. The surface vector is independent of the choice of which partitioning surface diagonal is used to define the cell volume with eight vertices. The volume is the dependent on which diagonal is based on each face, since the diagonal of four non-planar points do not intersect. An alternative formula has been given by Kordill and Virokul [24] which is particularly convenient as compared formula given by Davies [25], if the three required side vectors are stored. Evaluating the cell volume of general hexahedron but it is set against the advantage of the ease of fitting the cell together. A system of ordinary differential equations can be obtained by applying Eq. (5) to cells formed by six surfaces as

$$\Omega_{i,j,k} \frac{dU_{i,j,k}}{dt} + Q_{i,j,k} = 0 \tag{6}$$

where $\Omega_{i,j,k}$ is the volume of the cell, $Q_{i,j,k}$ is the convective fluxes out of the cell. The summation of the flux vectors over the six faces of the hexahedral cell is done using the average flux on each cell face. The above scheme reduces the centre differences scheme

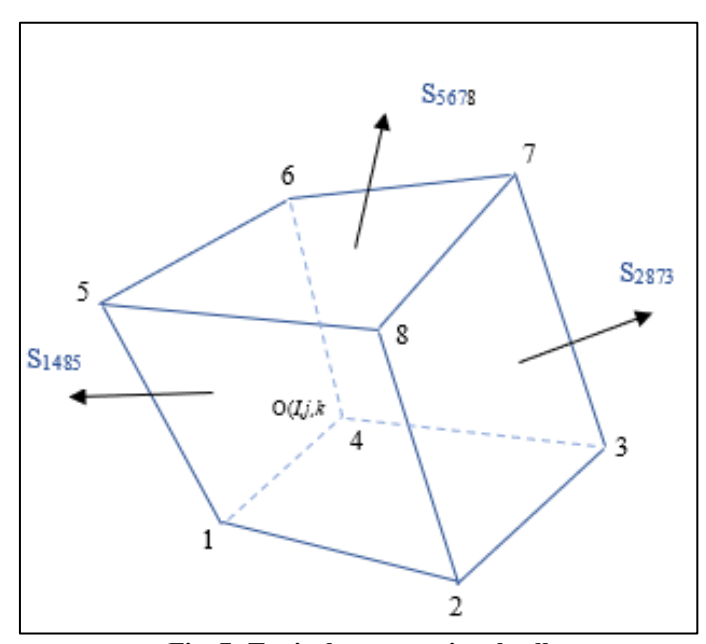


Fig. 7: Typical computational cell

2.8 Artificial Dissipation

In order to prevent odd-even point decoupling and oscillations in vicinity of shock waves, and to obtain rapid convergence to the steady state, artificial dissipative terms $D_{i,j,k}$ are added to Eq. (6). The artificial

dissipation model considered in the present paper is based on the work of Jameson *et al.*, [23]. A blend of forth and second differences is used to provide third-order back-ground dissipation at shock waves, and is given by

$$D_{i,j,k} = (D_x + D_y + D_k) W_{i,j,k}$$
 (7)

where

$$D_x U_{i,j,k} = d_{i+\frac{1}{2},j,k} - d_{i-\frac{1}{2},j,k}$$

The dissipative fluxes $d_{i+\frac{1}{m}j,k}$ are defined as blend in of first and third differences

$$d_{i+\frac{1}{2}j,k} = \frac{\Omega_{i+\frac{1}{2}j,k}}{\Delta t_{i+\frac{1}{2}j,k}} \left\{ \varepsilon_{i+\frac{1}{2}j,k}^{(2)} \left(U_{i+1,j,k} - \ U_{i,j,k} \right) - \ \varepsilon_{i+\frac{1}{2}j,k}^{(4)} \left(U_{i+2,j,k} - \ 3 U_{i,j,k} + 3 U_{i,j,k} - \ U_{i+1,j,k} \right) \right\}$$

The adaptive coefficients, $\varepsilon^{(2)}$ and $\varepsilon^{(4)}$ are

$$\varepsilon_{i+\frac{1}{2}j,k}^{(2)} = \kappa^{(2)} \max(\nu_{i+1,j,k}, \nu_{i,j,k})$$

$$\varepsilon_{i+\frac{1}{2},j,k}^{(4)} = \max\left\{0, \left(\kappa^{(4)} - \varepsilon_{i+\frac{1}{2},j,k}^{(2)}\right)\right\}$$

Here v is a shock sensing function based on pressure and can be written as

$$\nu_{i,j,k} = \frac{|p_{i+1,j,k} - p_{i,j,k} + p_{i-1,j,k}|}{|p_{i+1,j,k} + p_{i,j,k} + p_{i-1,j,k}|}$$
(8)

In the present computation the values of $\kappa^{(2)}$ and $\kappa^{(4)}$ are constants, taken equal to ½ and 1/256, respectively. The dissipative operators in the y and z directions are defined in a similar manner. The blend of second and fourth differences provided third-order background dissipation in smooth regions of the flow and first-order dissipation in shock waves.

2.9 Time-stepping scheme

The above spatial discretization reduces the governing equations to semi-discrete ordinary differential equations; temporal integration is carried out using multi-stage Runge-Kutta time-stepping scheme [23]. Suppressing the subscripts (i,j,k), the following steps are employed for the numerical integration

$$U^{(0)} = U^{n}$$

$$U^{(1)} = U^{n} - 0.6 \frac{\Delta t}{\Delta \Omega} \left(R^{(0)} - D^{(0)} \right)$$

$$U^{(2)} = U^{n} - 0.6 \frac{\Delta t}{\Delta \Omega} \left(R^{(1)} - D^{(0)} \right)$$

$$U^{(3)} = U^{n} - \frac{\Delta t}{\Delta \Omega} \left(R^{(2)} - D^{(0)} \right)$$

$$U^{n+1} = U^{(3)}$$

$$(9)$$

where n is the current time level, and n+1 is the new time level. R is the sum of the inviscid fluxes. In order to minimize the computation time, the evaluation of the dissipation term D is carried out only at the first stage, and then frozen for the subsequent stages. The numerical scheme is stable for a Courant number ≤ 2 . A local time step is used to get steady state solution.

2.10 Boundary conditions

Four types of boundary conditions are required for the computation of flow field, i.e., deflector surface, inflow, outflow, and symmetric conditions. They are prescribed as follows: At the deflector wall slip boundary condition is imposed and at the out-flow boundary, the two tangential velocity components are extrapolated from the interior, while at the inflow boundary they are specified as having far field values.

2.11 Dimension of Nozzle and double-wedge deflector model

The convergent-divergent nozzles were designed for producing jet exit M_e of 2.2 and 3.1 for the exit diameter D_e as described the above. The configuration of the jet deflector is described in Fig. 8.

The nozzle was having a semi-divergent cone angle of 15°. The jet deflector model consists of a cone apex angle of 70° and a tip blunt radius R_1 of $0.13D_e$. Further downstream a curvature of radius R_2 of $1.2D_e$ is provided at a location of $r = 0.7D_e$, where r is distance measured

from the model axis. The deflector has a base diameter of $8D_e$. Thus, two deflector model have been used, one being axisymmetric and the other being double-wedge deflector model having same geometrical profile..

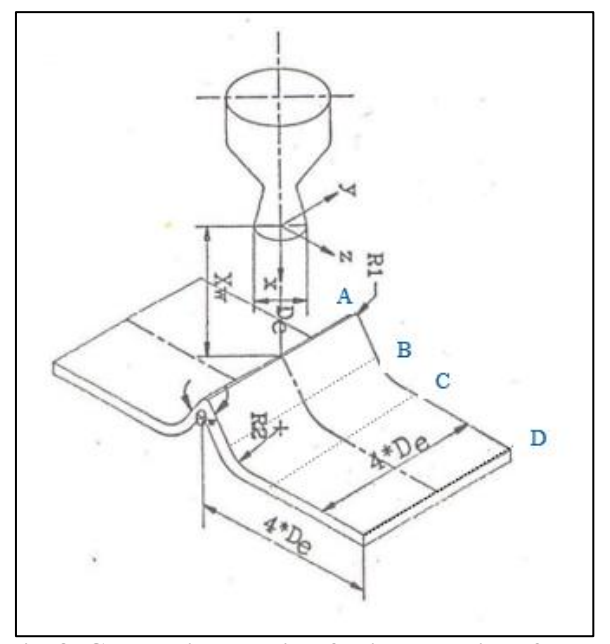


Fig. 8: Geometrical details of axisymmetric deflector

2.12 Computational grid over double-wedge deflector

Supersonic jets exhausting into a normally stationary external stream are computed using inviscid flow solver developed inhouse. The initial jet radius is equal to the exit radius i.e. equal to $0.5D_e$. A simple algebraic grid generation program is used to generate computational grid in computational domain a symmetric plane as depicted in Fig. 9. The finite element scheme is selected to generate multi-block structured method to divide the computational domain in 5 zones. The grid generation was carried out in two steps. Each of these blocks is considered as a super element, which is initially described by a single isoparametric finite elements [26]. The position of a plane inside an element

can be described in terms of a eight quadrilaterals. The grids are displayed in in Fig. 10(a) and (b) with the help of MATLAB software.

Due to axisymmetric nature of the problem, the computations are carried out on only one half of the jet. The computations were employed equally spaced grid points in the axial direction. Table 1 Operating parameters of nozzle and number grids used in doublewedge deflector. The convergence criterion to steady-state is taken (between two successive iterations) $|\rho^{n+1} - \rho^n| \le 10^{-4}$, where n is an iterative index. The steady-state is achieved after about 50000 iterations.

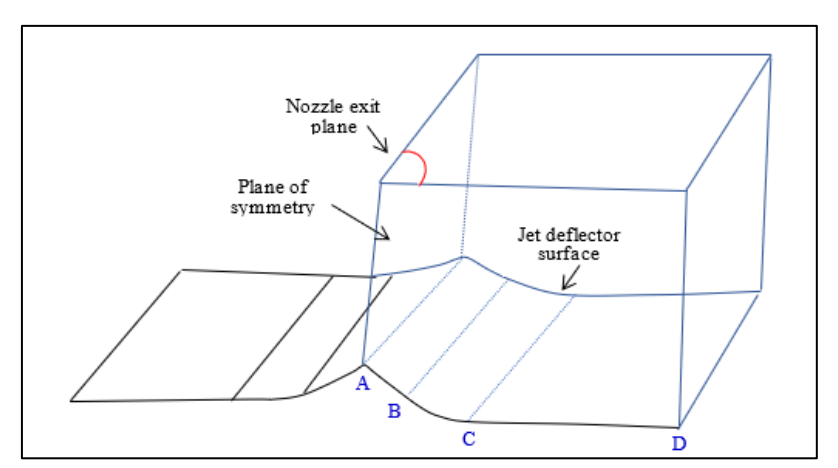


Fig. 9: Computational domain of the double-wedge deflector

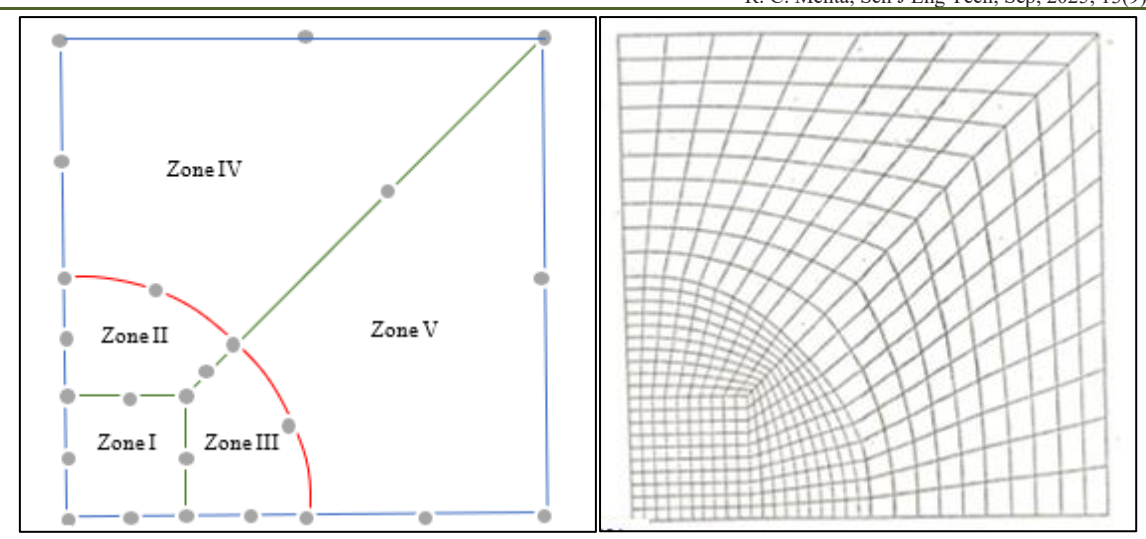


Fig. 10: Node points and grid on the top plane of the double-wedge deflector

Table 1: Operating parameters of nozzle and number grids used in double-wedge deflector

Test case	X_w/d_e	Me	p _e /p _a	Te ºK	nx×
					ny×nz
Job 1	3	3.1	0.8	266	34×51×22
Job 2	2	3,1	0.8	266	34×51×22
Job 3	4	3.1	0.8	266	34×68×22
Job 4	5	3.1	0.8	266	34×85×22
Job 5	3	2.2	1.0	252	34×85×22
Job 6	3	2.2	0.8	152	34×85×22
Job 7	3	2.2	0.6	152	34×51×22
Job 8	3	2.2	0.8	152	34×85×22
Job 9	3	2.2	1.2	152	34×51×22
Job 10	4	3.1	0.8	1026	34×68×22

3. Experimental facility

All the experimental simulations of supersonic free jet and jet deflector are conducted in an Open Jet Facility as shown in Fig.11. High pressure dry air at 4.3 \times 10^6 Pa at ambient temperature is fed through a 15×10^{-3} m diameter pipe line to the settling chamber and nozzle

assembly. A pressure regulating valve is used to control the operating pressure. The pressure in the settling chamber is continuously recorded and monitored using a Bourden pressure gauge and a pressure transducer. The experimental set up is coupled with data acquisition. The open jet facility can be operated continuously at the maximum pressure up to about 80 s.

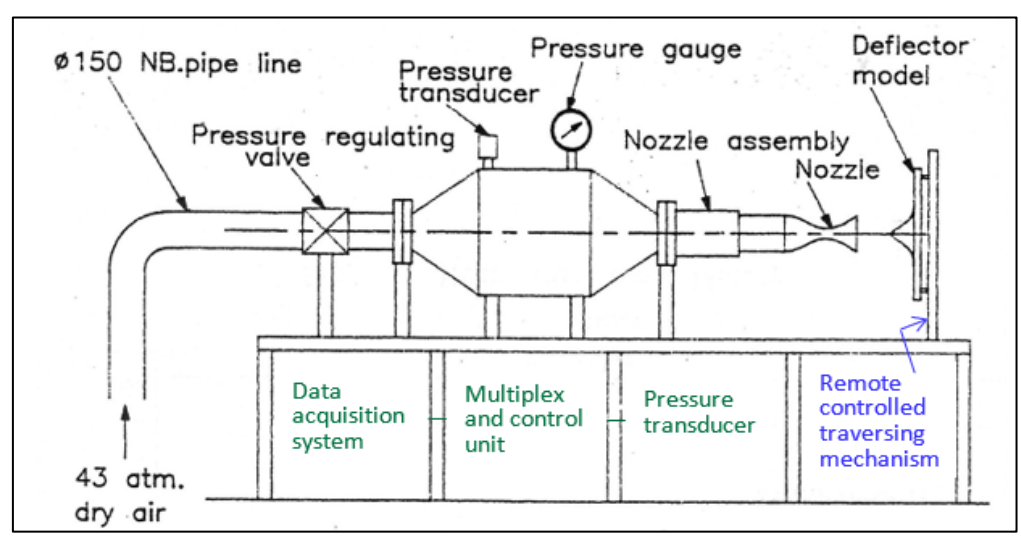


Fig.11: Experimental set-up of open jet facility

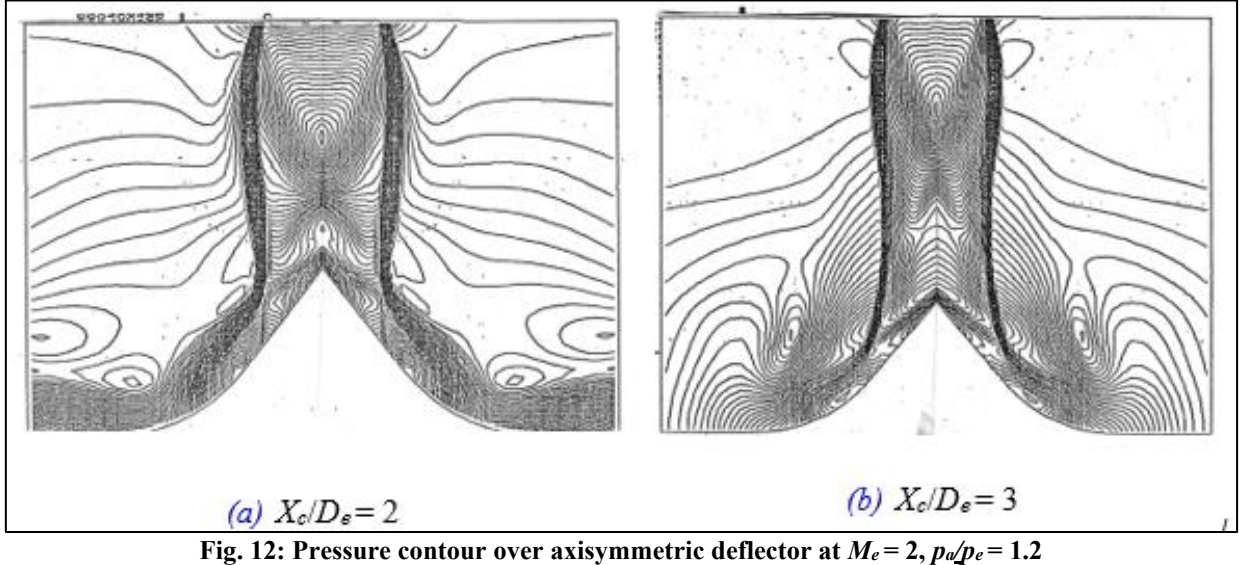
4. RESULTS AND DISCUSSION

The near field flow structures of a jet depend primarily on the operational conditions of the nozzle, which are characterized mainly by the Mach number of the jet at the nozzle exit and the ratio of the static pressure at the nozzle exit to the ambient static pressure, for either free jets or impinging jets. For impinging jets, the whole flowfield would also be affected by the impingement distance, i.e., the distance from the nozzle exit to the intersection point of the jet axis and the impinged surface. A nondimensionalized form is usually used, which is usually normalized by the nozzle exit diameter.

4.1 Flow structure over axisymmetric jet deflector

Distance between the nozzle exit plane and deflector apex is indicted as Xc and is nondimensionalized with nozzle exit diameter D_e . Pressure contour obtained from computations for $M_e = 2$, $p_a/p_e =$ 1.2 and $X_c/D_e = 2$ and 3 are shown in Fig. 12(a) and (b), respectively, over all flow patterns such as jet shock, triple point, slip line, reflected shock, apex shock, compression and expansion of flow near the axisymmetric deflector surface and wall jets clearly are clearly well captured. At $X_c/D_e = 2$, due to the presence of the deflector, free jet Mach disc has been displaced by about $0.14 D_e$. A weak compression region is seen in the vicinity of the deflector apex, attribute to the prevailing low speed flow downstream of the Mach disc. Several compression and expansion regions appeared downstream of the deflector attributed to the multiple reflection of the above expansion waves from the deflector surface and jet boundary as shown in Fig. 2. With increase $X_c/D_e = 3$, the deflector in the influence of second shock cell. The flowfield has altered significantly as seen in Fig. 12(b) compared to the flow structure as $X_c/D_e = 2$ of Fig. 12(a). the cone shock joins the jet boundary and reflected as expansion fans. It is important to mention here that the overall impingement flow structure is remain similar to the case of $X_c/D_e = 2$. In other words, all the above flow characteristics indicate that the impingement flow field alters appreciably with change in X_c/D_e .

However, the comparison between pressure contour of the supersonic jets with impinging supersonic jets on axisymmetric differs considerably different. The inner mixing layer of the impinging supersonic jets is different at different nozzle operating parameters such as expansion ratio, nozzle exit Mach number and distance between nozzle to the deflector surface. The difference in the velocity field may cause to the formation of the vortex.



4.2 Static pressure distribution for $M_e = 2.2$ and p_e/p_a = 1.2 at $X_c/D_e = 2, 3$ and 5

The marking A, B, C and D in the radial direction show the deflector apex, starting and end ending of the downstream deflector curvature and corner of the deflector, respectively. Static pressure distributions on axisymmetric deflector for $M_e = 2.2$ and $p_e/p_a = 1.2$ at $X_c/D_e = 2$, 3 and 5 are depicted in Fig. 13. Pressure variation up to $r/D_e = 0.15$ remains unchanged. Further downstream along the deflector surface, seen increase in pressure indicate presence of compression.

After words, the pressure decrease due to acceleration of the flow. At last, pressure decreases to the ambient pressure pa attributed to mixing of the flow with ambient. The pressure variation for $X_c/D_e = 3$, indicates maximum value at the point A and is higher than the stagnation pressure for $X_c/D_e = 2$. It will give rise to a static pressure across the apex shock lower than at the point A. The increase in pressure at $X_c/D_e = 3$ is identical to the case of X_c/D_e =2. With further increase to distance to X_c/D_e =5, the pressure at the stagnation point has decreased as compared to $X_c/D_e = 2$.

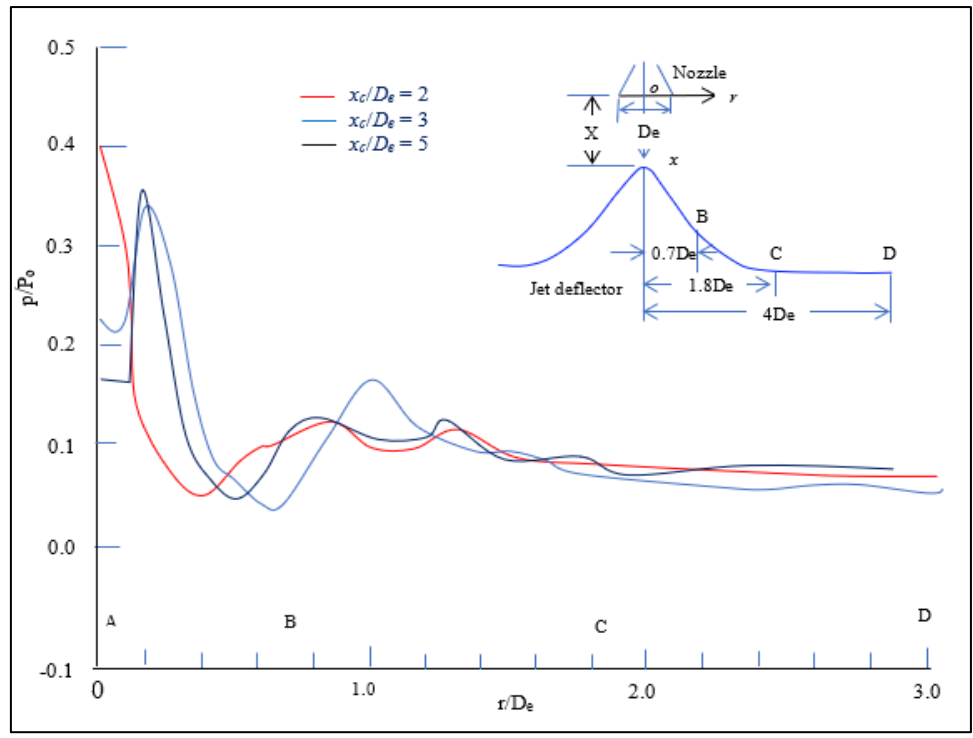


Fig. 13: Static pressure distributions on axisymmetric deflector at various X_C/De for $M_e = 2.2$ and $p_e/p_a = 1.2$

4.3 Static pressure distribution for $M_e = 2.2$, $X_c/D_e = 2$ for $p_e/p_a = 1.2$, 1.0 and 0.8

Static pressure variations on the axisymmetric deflector surface for $M_e = 2.2$, $X_c/D_e = 2$ at different expansion ratio $p_e/p_a = 1.2$, 1.0 and 0.8 are depicted in Fig. 14. It can be observed from pressure distribution changes with change in expansion ratio p_e/p_a . with

decreases in expansion ratio p_e/p_a from 1.2 to 0.8, the stagnation point A pressure increase. However, it appears to decrease with p_e/p_a . At $p_e/p_a = 1$, pressure distribution decreases from the stagnation point A due to acceleration of flow downstream for $X_c/D_e = 2$. The characteristic of pressure variation downstream is identical to the case of $p_e/p_a = 1.2$.

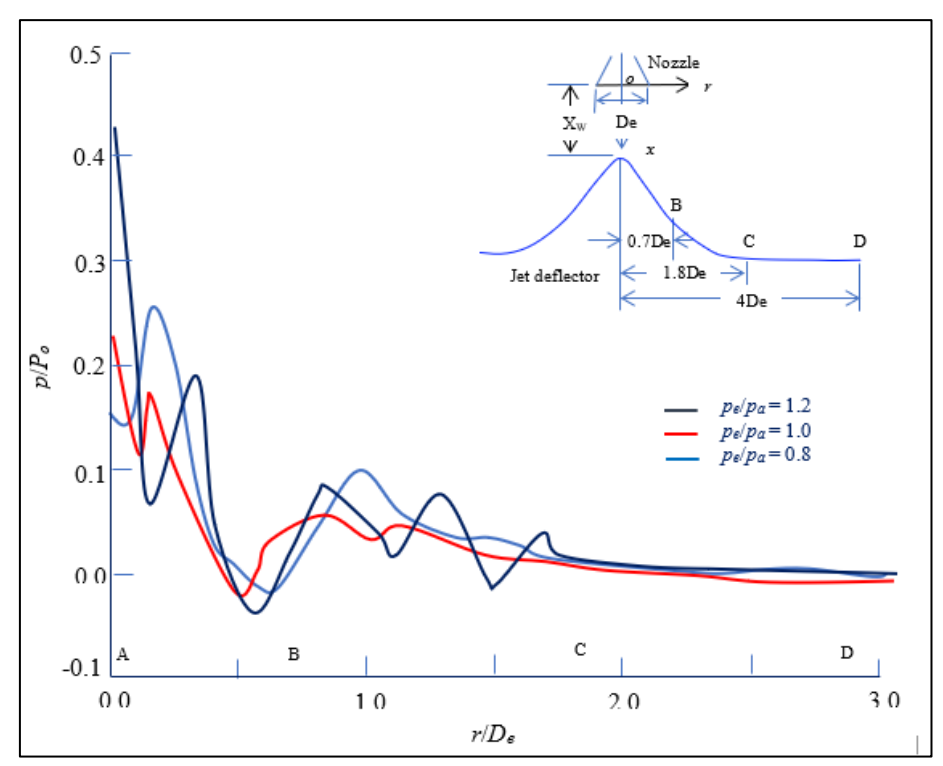


Fig. 14: Static pressure distributions on axisymmetric deflector at various expansion ratio for $M_e = 2.2$ and $Z_C/D_e = 2$

4.4 Static pressure on the stagnation point

Centre line pressure variations in the presence of the deflector are shown in Fig. 15 at different operating parameters. The static pressure distribution on the centre line of the axisymmetric deflector with respect to the nozzle is nondimensionalized by settling chamber pressure P_o and r is nondimensionalized by the nozzle exit diameter D_e . A sharp rise of the pressure on the stagnation point A of the deflector.

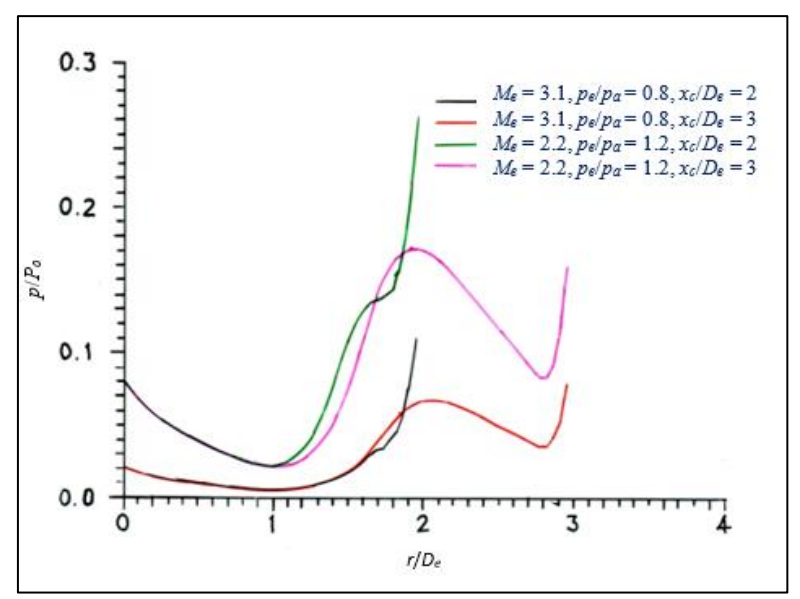


Fig. 15: Centre line pressure distribution in the presence of axisymmetric jet deflector

5. Flow field over double-wedge deflector

Flow field over double-wedge deflector is analysed for various operating parameters as given Table 1 for double-wedge jet deflector. The dimension of the axisymmetric and the double-wedge deflector models are similar as depicted in Figs. 5 and 8. It will make convenient to compare results of the axisymmetric deflector with the double wedge deflector under identical operating conditions.

5.1 Impingement Flowfield on a double wedge deflector

Mach contour of impingent flowfield for $M_e = 2.2$ and $p_e/p_a = 1.2$ at different distance $Z_c/D_e = 2, 3, 4$ and 5 and corresponding schlieren pictures, respectively, are shown in Fig. 16 (a) and (b). All the essential flowfields features are captured well and compared well with the schlieren pictures. Mach contour pictures changes flowfield as a function of Z_c/D_e as lift-off of satellite launch vehicle. Flow field of impinging jets on a double-wedge deflector as the satellite launch vehicle lifts off. The colour contour picture shows how flowfield alters as lift of vehicle.

For $Z_c/D_e = 2$, the wedge apex is downstream pf the first Mach disc. Location of the Mach disc is slightly displaced upstream with its downstream and its core of the jets has increased. A weak wedge shock is formed because the flow spreading the deflector has become supersonic. The flow expands due to acceleration downstream of the wedge apex and further downstream, compared due the deflector curvature is seen, and a wall jet along the deflector surface is formed. For $Z_c/D_e = 3$, a

detached wedge shock is appeared because the incoming flow has achieved supersonic speed. The wedge shock joins the jet boundary and the jet boundary gets deflected outward due to expansion at this point. A shock downstream of the apex is also noticed. $Z_c/D_e = 4$, the wedge shock takes the shape of a Mach disc and the flowfield is identical to the flowfield as observed for $Z_c/D_e = 2$. Further displacement of the deflector from the nozzle exit plane for $Z_c/D_e = 5$, a wedge shock is appeared because the incoming flow achieved the supersonic speed.

The above flow field features are compared with the schlieren pictures [27] for $Z_c/D_e = 2$ and 4 indicate similarity. In both these cases the deflector apex is downstream of the Mach disc. Similarly, when the deflector is placed downstream of the shock cell, similar flowfield characteristics is seen for $Z_c/D_e = 3$ and 4.

As shown in Fig. 16, during the rocket launching, the flowfield of engine exhaust impingement behaves differently at varying lift-off heights, which is defined as the distance between the nozzle exit and the launch platform. he flowfield over the rocket changes dynamically during its lift-off stage. As illustrated in Fig. 16, by varying the impingement distance and taking the pressure ratio and jet Mach number fixed, the distance between the standoff shock and the plate, as well as the locations of the shock cells upstream of the standoff shock, is almost constant. As shown in Fig. 16, during the rocket launching, the flow field of engine exhaust impingement behaves differently at varying lift-off heights, which is defined as the distance between the

nozzle exit and the launch platform. The schlieren pictures are taken from Ref. 27. Thus, the flow field over the rocket changes dynamically during its lift-off stage. When the rocket starts to ascend, the engine exhaust impinges onto the launch platform and produces

complex flow structures nearby. During this stage, the engine exhaust mainly interacts with the launch platform or the deflector system. As the rocket ascends further, the interaction between the engine exhaust and launch structures becomes weaker.

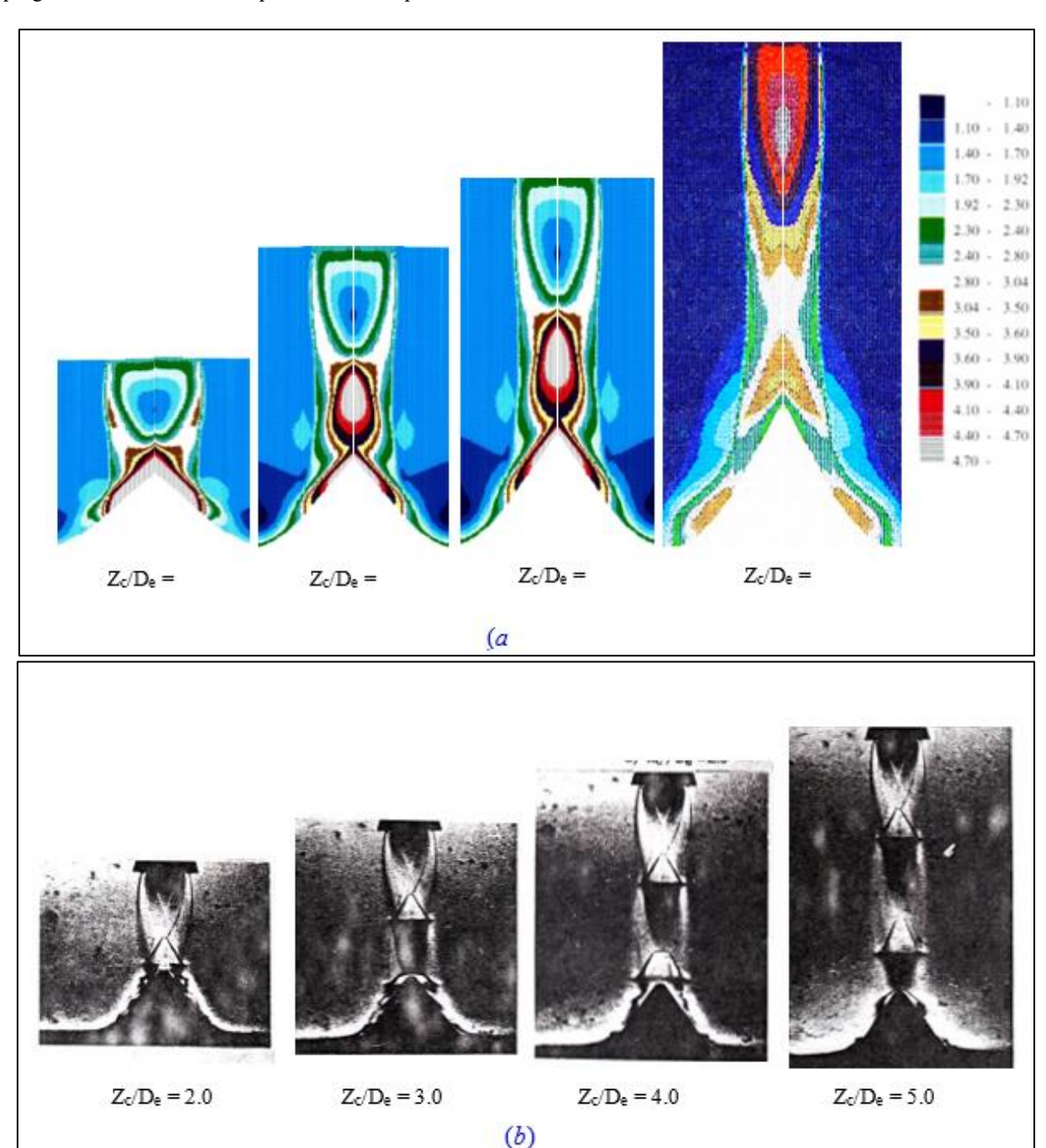


Fig. 16: Mach contour and schlieren picture over double-wedge deflector at $M_e = 2.2$ and $p_e/p_a = 1.2$ for different $Z_c/D_e = 2, 3, 4$ and 5

5.2 Mach distribution over double-wedge deflector for various operating conditions

Figure 17 (a), (b), (c), (d) and (e) are displayed Mach number distribution over double-wedge deflector

for different values of $X_w/D_e = 3$, $M_e = 3.1$, $p_e/p_a = 0.8$, $X_w/D_e = 4$, $M_e = 3.1$, $p_e/p_a = 0.8$, $X_w/D_e = 5$, $M_e = 3.1$, $p_e/p_a = 0.8$, $X_w/D_e = 3$, $M_e = 2.2$, $p_e/p_a = 0.6$, and $X_w/D_e = 3$, $M_e = 2.2$, $p_e/p_a = 1.2$, respectively.

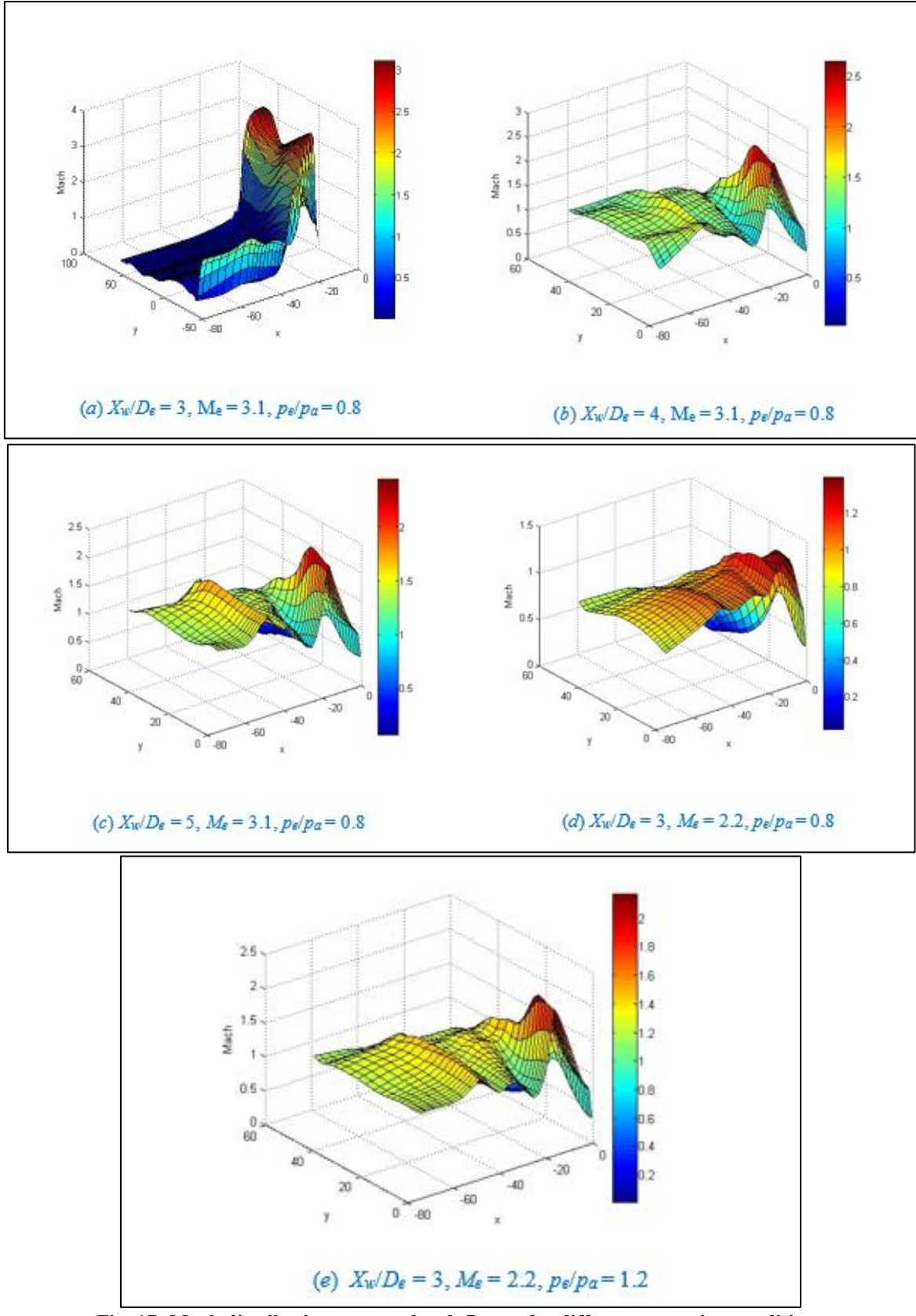


Fig. 17: Mach distribution over wedge deflector for different operating conditions

The main purpose is to show three-dimensional Mach number distributions over the double-wedge deflector. It can be seen from the figures that the effect of operating parameters over the double-wedge

deflector. Mach number over the apex of the double-wedge deflector is significant and function of X_w/D_e , M_e and p_e/p_a .

5.3 Static pressure distribution for $M_e = 2.2$

Figure 18 shows variations of static pressure on centre line of double-wedge deflector $M_e = 2.2$ and $p_e/p_a = 1.2$ for different values of $X_w/D_e = 2$, 3 and 5. At $X_w/D_e = 2$, pressure falls gradually from point A up to about $X_w/D_e = 0.26$, where a compression is found and further downstream, is again falls due to flow acceleration till compression initiated due to presence of the model downstream till point C. After the compression pressure starts to fall due to mixing of the wall jet with atmosphere. For $X_w/D_e = 3$, pressure decrease sharply

from point A up to $X_w/D_e = 0.1$ this attributed formation of weak shock. For $X_w/D_e = 5$, the pressure decreases continuously along the deflector surface till compression due to deflector curvature take place. It is observed that the change in pressure variation, is confined to within a region of half nozzle diameter. From the deflector axis. In all the numerical simulations of X_w/D_e , the minimum pressure appears to occur at $X_w/D_e = 0.8$ and is lower than the p_a . Maximum pressure downstream of the doublewedge deflector curvature reaches almost to the same value for all X_w/D_e .

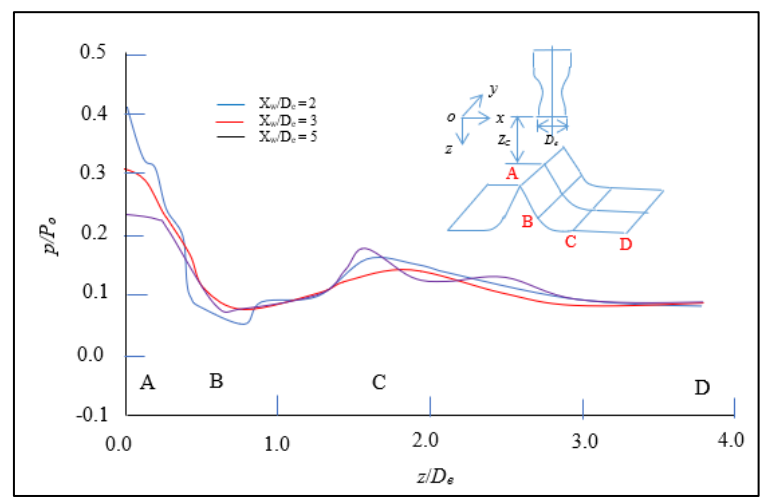


Fig. 18: Static pressure distributions on centre line of wedge deflector at various X_c/D_e for $M_e = 2.2$ and $p_e/p_a = 1.2$

Figure 19 shows static pressure distributions on centre line of double-wedge deflector for $M_e = 2.2$ and $X_w/D_e = 2$ and at various values of $p_e/p_a = 1.2$, 1.0 and 0.8. The pressure distribution reveals the effect of expansion ratio for fixed value of exit Mach number and distance from nozzle exit plane to deflector. At $p_e/p_a = 1.2$, the expansion downstream of double-wedge apex is

gradually decreases up to $X_w/D_e = 0.3$. The stagnation pressure is high at $p_e/p_a = 1.0$ compared to $p_e/p_a = 1.2$. at $p_e/p_a = 0.8$, the stagnation point A pressure is close to the value for $p_e/p_a = 1.0$, and downstream characteristic of pressure variation is identical to the characteristic for $p_e/p_a = 1.0$. At $p_e/p_a = 0.8$, the pressure variation is again identical to the downstream as $p_e/p_a = 1.2$.

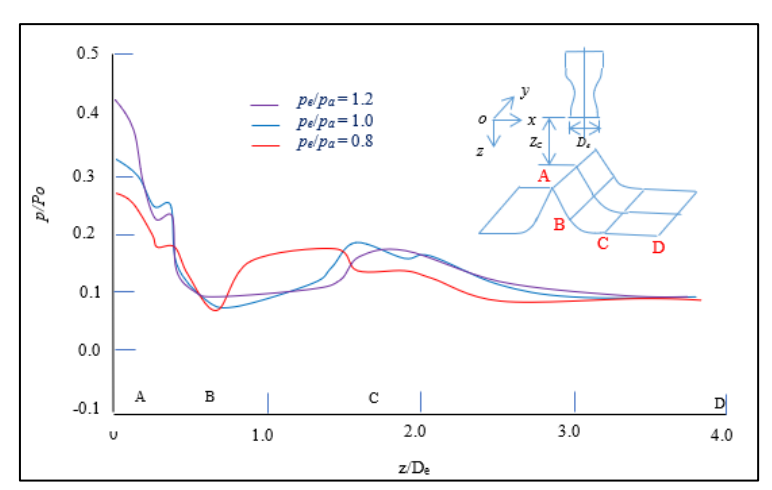


Fig. 19: Static pressure distributions on centre line of double-wedge deflector for $M_e = 2.2$ and $X_w/D_e = 2$ at various values of $p_e/p_a = 1.2$, 1.0 and 0.8

The effect of exit Mach number $M_e = 2.2$ and 3.1 on static pressure distribution is analysed in Fig. 20. It is seen from the pressure variations that the influence

of double-wedge deflector downstream curvature, shown by the pressure rise, is higher at the lower jet Mach number

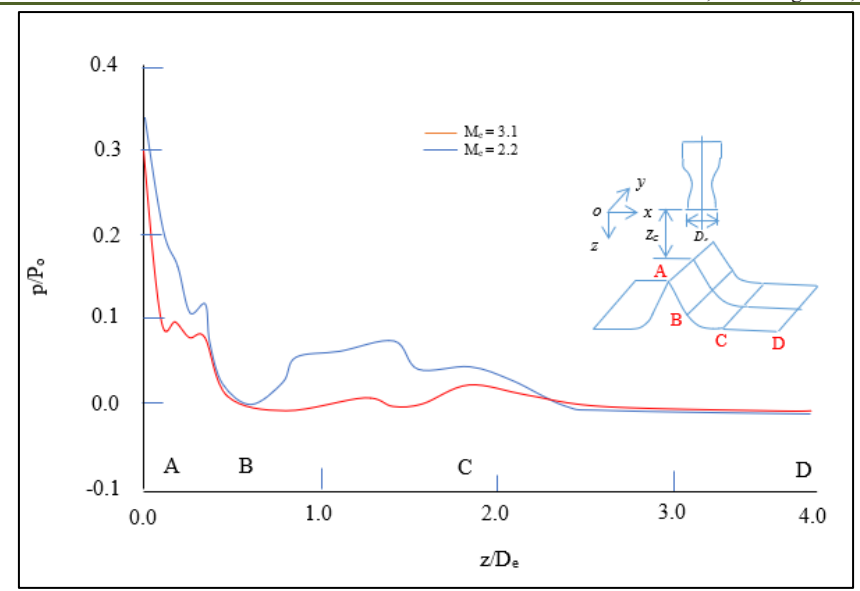


Fig. 20: Effect of jet Mach number on pressure distribution over wedge deflector at $X_W/De = 2$ and $p_e/pa = 0.8$

5.4 Spanwise pressure distribution for $M_e = 2.2$

Static pressure computed on a double-wedge deflector surface along the centre-line of the deflector in the spanwise direction in Fig. 21 for $M_e = 3.1$, $X_W/D_e = 3$ and $p_e/p_a = 0.80$. it is observed that the pressure distributions along the deflector surface are identical at

Y/De = 0.011, 0.22 and 0.4, except the minor pressure fluctuation on the wedge surface which may be due the three-dimension nature of the flow. This pressure variation can be integrated to determine the impingement load on the double wedge deflector.

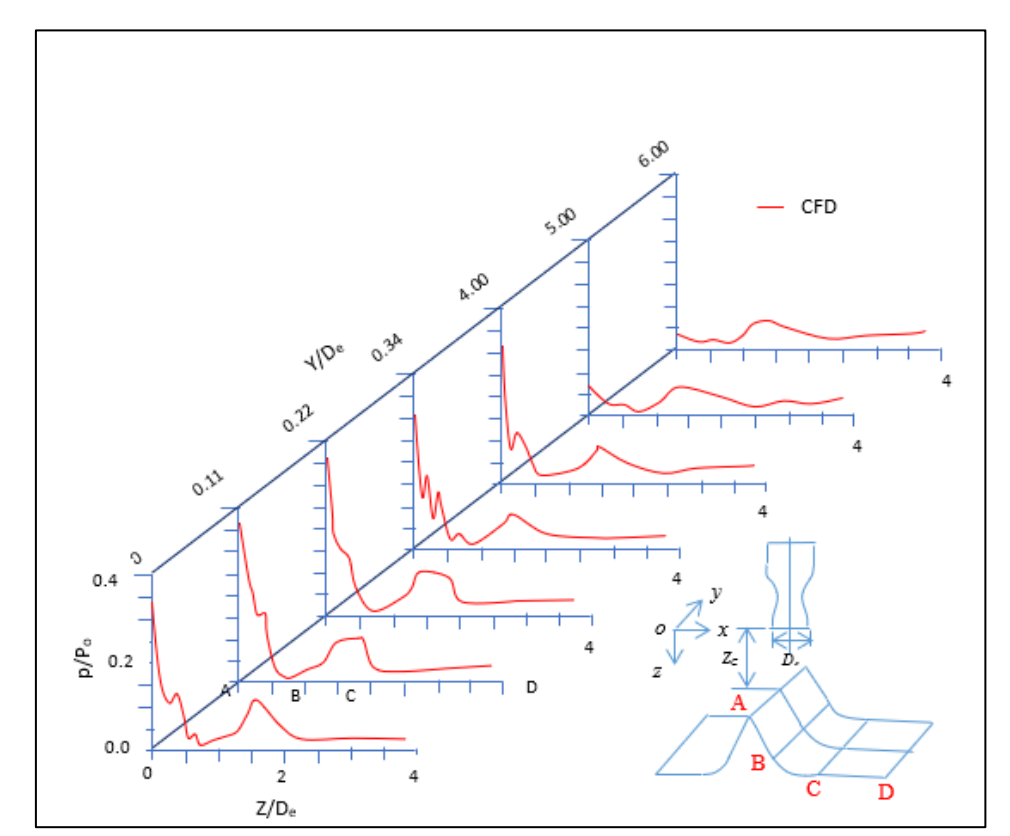


Fig. 21: Spanwise pressure distributions on wedge deflector for $M_e = 3.1$, $X_W/D_e = 3$ and $p_e/p_a = 0.80$

5.5 Comparison of pressure distribution between axisymmetric and double-wedge deflector

Due to the impingement of supersonic axisymmetric jet on an axisymmetric deflector is

axisymmetric. However, when it impinges on a doublewedge deflector, the impingement flowfield will be three-dimensional nature but symmetric normal to flow direction. Flowfields are to be different span-wise direction. Figure 22 shows pressure the comparison between them for $M_e = 2.2$ and $p_e/p_a = 1.2$ for various values of X_w/D_e . It is found that effect of the downstream

curvature (point B and C) is less in the case of axisymmetric deflector.

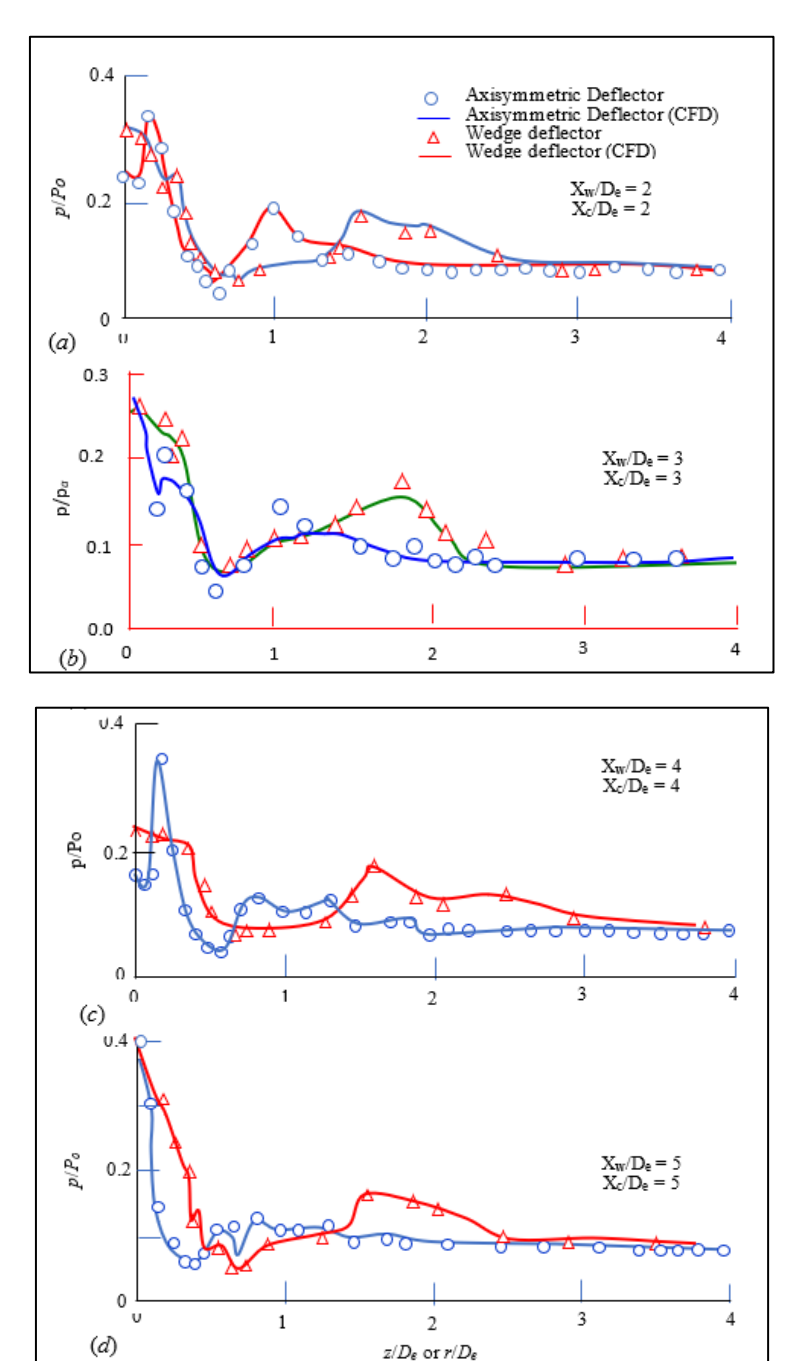


Fig. 22: Comparison of static pressure distribution on axisymmetric and double-wedge deflectors for $M_e = 2.2$ and $p_e/p_a = 1.2$

CONCLUSIONS

Numerical analysis of cold air emanating from convergent-divergent nozzles have been carried out. The studies consisted of density, pressure and Mach contour flow visualization and measurement of static pressure distributions on deflector surface. In these computations, the jet exits $M_e = 2.1$ and 3.1 and $p_e/p_a = 0.6 - 1.2$, $T_o = 300^{\circ}$ K, $x/D_e = 2$ to 5 and y = 1.4.

Comprehensive numerical investigations have been carried out to obtain the impingement flowfield of a jet deflector by computing surface pressure and flow visualization. Distance between the nozzle and the deflector has been varied in the range of 2 to 5 times the nozzle exit diameter.

The axisymmetric cone-shaped and doublewedge shaped deflectors have different diversion directions of exhaust gases emanating from nozzle. Compared to the wedge-shaped deflector, the coneshaped deflector could achieve better performance for deflecting with sufficient distance of the sidewalls.

The location of maximum static pressure increases with the increase in expansion ratio. This indicates that flame deflector tests should be carried out at different range of stand-off distances depending upon the expansion ratio p_e/p_a of the nozzle.

Nomenclature

1	10 0 7 7 1 0 0 V 1 f	cross-sectional	0400
A_{e}	HOZZIE EXII	. CLOSS-SECTIONAL	area

 A^* nozzle throat area nozzle exit diameter

 D_e

 d^* Nozzle throat diameter

е specific total internal energy

F, G, H inviscid flux vector

exit nozzle design Mach number M_e

stagnation pressure P_o

pressure p

pressure at the nozzle exit p_e

ambient static pressure p_a

first shock cell length L_1

radial coordinate

S source vector

 T_o stagnation temperature

velocity components *u*, *v*, *w*

Uconserved vector quantity

x or Zaxial distance from the nozzle exit plane

density ρ

 θ deflector apex angle

ratio of specific heats γ

REFERENCES

- 1. Anon. Acoustic Loads Generated by the Propulsion System, Langley Research Centre, Hampton Virginia, USA, NASA SP-8072, 1971
- Cobbald, T. J., The impingement of underexpanded, axisymmetric, rocket motor exhausts and cold jets on flat plates, Ph. D. thesis, University of Bristol, U.K., 1985.
- Evans, R. L. and Sparks, O. L., Launch Deflector Design Criteria and Their Applications, George C. Marshall. Space Flight Center Huntsville, Alabama, NASA TN D 1275, 1963
- 4. Dordain, J. J., Firing-tests of a model of the Ariane launch vehicle, Acta Astronautica, 4(5 - 6), 1977, https://doi.org/10.1016/0094-727-748, 5765(77)90117-5.
- Lamont, P. J., Hunt, B. L., The Impingement of Axisymmetric Underexpanded, Jets Perpendicular and Inclined Flat Plates, Journal of Fluid Mechanics, 100(3),1980, 471–511. doi:10.1017/S0022112080001255
- 6. Nakai, Y., Fujimatsu, N., and Fujii, K., Flow Classification of the Under-Expanded Super Sonic Jet Impinging on a Flat Plate, AIAA Paper 2003-3467, 2003.
- 7. Nakai, Y., Fujimatsu, N., and Fujii, K., Experimental Study of Underexpanded Supersonic

- Jet Impingement on an Inclined Flat Plate, AIAA Journal, 2006, 2691-2699 (11),doi:10.2514/1.17514
- Zhou, Z, Zhao, C, Lu, C., and Le, G., Numerical studies on four-engine rocket exhaust plume impinging on flame deflectors with afterburning. Defence Technology. 2021; 17: 1207-1216.
- Jiang, C, Han, T., Gao, Z., Lee, C., A review of impinging jets during rocket launching. Prog Aero 2019;109. doi.org/10.1016/j.paerosci.2019.05.007.
- 10. Zhou Z, Zhang L, Le G: Numerical study for the flame deflector design of four-engine liquid rockets, Engineering Applications of Computational Fluid 2020:14: DOI:10.1080/19942060.2020.1761453
- 11. Wu J, Lin T, Luke, EA, Tong X, Cinnella P: Comprehensive numerical study of jet-flow impingement over flat plates. Journal of Spacecraft and Rockets. 2002; 39: 357-366. doi.org/10.2514/2.3834
- 12. Kim K. H. and Chang K. S., Three-dimensional structure of a supersonic jet impingement on an inclined plate, Journal of Spacecraft and Rockets, 31, 1984, 778-782. doi.org/10.2514/3.26512
- 13. McIlroy K, and Fujii K., Computational analysis of supersonic underexpanded jets impinging on an inclined flat plate. AIAA Paper 2007-3859, 2007 https://doi.org/10.2514/6.2007-3859
- 14. Zhou, Z. T., Zhao, C. F., Lu, C. Y., and Le, G. G., Numerical studies on four-engine rocket exhaust plume impinging on flame deflectors with afterburning, Defence Technology 17, 2021 1207e1216, https://doi.org/10.1016/j.dt.2020.06.016
- 15. Karthikeyan, N. and Venkatakrishnan, L., Acoustic Characterization of Jet Interaction with Launch Structures During Lift-Off, Journal of Spacecraft and Rockets. 54(2), 2017, 356-367
- 16. Brehm C., Sozer E., Moini-Yekta S., Housman J.A., Kiris C., Barad M. F., Vu B. T., and Parlied C. R., Computational prediction of pressure environment in the flame trench with launch vehicles. 31st AIAA Applied Aerodynamics Conference; 2013.
- 17. Akamine M., Okamoto K., Gee K. L., Neilsen T. B., Teramoto S., Okunuki T., and Tsutsumi S., Effect of nozzle-plate distance on acoustic phenomena from supersonic impinging jet. AIAAJ, 56, 2018. https://doi.org/10.2514/1.J056504
- 18. Prasad, J. K., Mehta, R. C. and Sreekanth, A. K., Impingement of supersonic jets on axisymmetric deflector, AIAA Journal, 32(7) 1994, pp. 1535-1538
- 19. Prasad, J. K., Mehta, R. C. and Sreekanth, A. K., Experimental Study of overexpanded supersonic jet impingement on a double wedge deflector. The Aeronautical Journal of the Royal Society, 1997, pp, 209-214
- 20. Mehta, R. C., Numerical Simulation of Double Wedge Supersonic Jet Deflector, Computer Fluid Dynamics Journal, 18(1) 2009, pp. 31-36

- Mehta, R. C., Analysis of Supersonic Free Jets and Impinging Supersonic Jets, Simulation Modeling, Recent Advances, New Perspectives, and Applications, 2024 DOI: 10.5772/intechopen.1002372
- 22. Jiang, C., Han, T., Gao, Z. and Lee, C. H., A review of impinging jets during rocket launching, Progress in Aerospace Sciences, 109, 2019, 100547 https://doi.org/10.1016/j.paerosci.2019.05.007.
- Jameson, A., Schmidt, W., and Turkel, E., Numerical Simulation of Euler Equations by Finite Volume Methods Using Runge-Kutta Time Stepping Schemes, AIAA paper 81-1259, June 1981.
- 24. Kordulla, W. and Vinokur, M., Efficient computation of volume in flow predictions, AIAA

- Journal, 21(4), 1983, 917-918 https://doi.org/10.2514/3.8174
- Davies, D. E. and Salmond, D. J., Calculation of the volume of a general hexahedron for flow predictions, AIAA Journal, 23(6), 1985, 954-956 https://doi.org/10.2514/3.9013
- 26. Mehta, R. C., Multi-Block Structured Grid Generation for Computational Fluid Dynamics, Scholar Journal of Engineering and Technology, 5(8), 2017, 87-219 DOI: 10.21276/sjet
- 27. Prasad J. K. and Kutty C. S., Impingement on PSLV jet deflector: cold flow simulation test results, Aerothermal Test Facilities, ATTF:07:85, Trivandrum, October, 1985